Chaos
An Interdisciplinary Journal
of Nonlinear Science

AIP Publishing

Feynman-Kac equation for microtubule search process in prometaphase

Heng Wang,[1] Yayun Xue,[1] and Weihua Deng[1]
School of Mathematics and Statistics, State Key Laboratory of Natural Product Chemistry, Lanzhou University, Lanzhou 730000, P.R. China.

(*Electronic mail: dengwh@lzu.edu.cn)

(Dated: 18 December 2025)

In prometaphase, microtubules form the spindle structure through dynamic instability, accurately locating and capturing chromosomes to ensure the equal distribution of genetic material (DNA on chromosomes). In this paper, we establish a dynamic model of the microtubule growth-rotation search process by considering the non-local polymerization and depolymerization of microtubules affected by mechanisms such as katanin proteins and kinetochore fibers, and derive the macroscopic equation for the microtubule-kinetochore capture model by imposing appropriate boundary conditions. Further, we derive the Feynman-Kac equations that govern the probability density of the functional for the microtubule growth-rotation search model. Finally, we validate the derived equations by comparing results from using deep learning method to solve the equations with those from applying Monte Carlo simulations to the microscopic models.

In prometaphase, microtubules form the spindle through dynamic instability, efficiently searching for and capturing chromosomes to ensure the normal progression of mitosis[1–3]. Till now, it seems that the molecular mechanism underlying this process has not been very well understood. The progress includes that the growth-rotation model is an effective framework for characterizing the microtubule's search process[4–6]. By adjusting the intensity parameters of growth and rotation motion, this model can characterize the microtubule's search process in different cell types[7]. Microtubules are linear polymers formed by the polymerization of tubulin dimers, which consist of α-tubulin and β-tubulin. Each dimer has a length of approximately 8 nm[7], while the average length of microtubules varies from 1 μm to 50 μm across different cell types[8]. Furthermore, the growth dynamics of microtubules are regulated and influenced by multiple factors, such as the cleavage by katanin proteins[9] and kinetochore fibers[10]. Here we develop a more detailed non-local polymer model for microtubule search process. The establishment of the polymer model and the capture of chromosomes by microtubules both result in a high-dimensional coupling system[11–13]; thus, it is crucial to use deep learning as a tool to effectively solve such models[14–19]. This paper focuses on investigating the dynamic models of the polymerization-depolymerization growth-rotation search process of microtubules in small-scale cells, as well as the corresponding Feynman-Kac equations and the macroscopic equation for the microtubule-kinetochore capture model.

I. INTRODUCTION

Cell division enables eukaryotic cells to grow and reproduce, involving the nuclear process of mitosis and the cytoplasmic process of cytokinesis. Mitosis consists of five stages: prophase, prometaphase, metaphase, anaphase, and telophase. During mitosis, chromosomes (the primary carriers of genetic information) undergo a series of orderly changes to ensure their accurate segregation. This precise transmission of genetic material from parent to daughter cells supports the normal growth and development of organisms, as well as the continuity and stability of species. Prometaphase represents a critical stage in chromosome segregation[20]. During this phase, microtubules capture the kinetochores on chromosomes and exert regulated forces; through a series of regulatory mechanisms[10,21–25], chromosomes align on the equatorial plate, ensuring their equal partitioning into two daughter cells. However, factors such as cell morphology and erroneous microtubule-kinetochore interactions may result in unequal chromosome distribution, which contributes to the onset of various diseases, including developmental disorders[26,27], cancer[28], and age-related conditions[29]. The molecular mechanisms underlying microtubule-kinetochore capture remain incompletely understood. Elucidating the mechanism of microtubule-kinetochore capture is therefore of particular importance, as it deepens our understanding of disease pathogenesis and provides new perspectives for clinical diagnosis and treatment.

The search and correct capture of kinetochores by microtubules is crucial for their proper distribution into daughter cells. Mitchison et al. first propose that dynamic instability is a general property of microtubules and may be fundamental in explaining cellular microtubule behavior[1]. This finding indicates that microtubules elongate stably when they possess a GTP-tubulin cap and undergo rapid shortening when this cap is lost (becomes to GDP-tubulin). Walker et al. investigate the effect of tubulin concentration on microtubule growth and shrinkage rates[30], showing that microtubules switch randomly between elongation and rapid shortening states. Moreover, an increase in tubulin concentration reduces the frequency of transition from elongation to rapid shortening, while increasing the rescue frequency (the transition from rapid shortening back to elongation). McNally et al. identify proteins in eukaryotic cells that induce catastrophic collapse events[9]. Based on dynamic instability, Holy et al. model microtubules as rigid rods that capture kinetochores through random growth in all directions[2]. Kalinina et al. simplify microtubule dynamics into three states: growth, plateau, and shrinkage, and establish a rotation search-and-capture model for microtubules[31]. Nayak et al. compare different mechanisms to investigate cap-

ture characteristics in various cell types, providing a theoretical basis for model selection[7].

Modern microscopy techniques enable the observation of mean squared displacement (MSD) with power-law correlation[32,33] $\mathbb{E}\left[x(t)^2\right] \sim t^\alpha$, including subdiffusion with $0 < \alpha < 1$, normal diffusion with $\alpha = 1$, and superdiffusion with $1 < \alpha < 2$. Normal diffusion typically exhibits a normal (Gaussian) probability density function; however, recent studies reveal the phenomenon of "Brownian yet non-Gaussian" diffusion, where the MSD is proportional to time $\mathbb{E}\left[x(t)^2\right] \sim t$, but the probability density function is non-Gaussian[34]. The center of mass of linear polymers undergoing polymerization and depolymerization also exhibits this behavior[35], and the model is expressed as

$$dx(t) = \sqrt{2D(n(t))}dB(t), \tag{1}$$

where $D(n(t))$ depends on the polymer length $n(t)$, and $B(t)$ is standard Brownian motion. Nampoothiri et al. discuss polymer motion in a chemostatted monomer bath with changing monomer concentration[36].

In experiments, one typically measures the physical observable $A(t)$, whose time evolution is determined by the underlying dynamical process $Y(t)$ of the system. Such time-extensive quantities are usually expressed as functionals of the underlying process, which takes the form

$$A(t) = \int_0^t U(Y(s))ds. \tag{2}$$

Here, $U(x) \in \mathbb{R}$ is a prescribed arbitrary function, which is determined by the observable in the specific application scenario. To obtain the probability density of $A(t)$, one needs to consider the quantities $\tilde{p}(y,p,t) = \mathbb{E}\left[e^{-ipA(t)}\delta(y-Y(t))\right]$ and $\tilde{p}_{y_0}(p,t) = \mathbb{E}\left[e^{-ipA(t)}; Y(0) = y_0\right]$, which can be obtained by solving the forward and backward Feynman-Kac equations, respectively. In the linear case $U(x) = x$ and $Y(t)$ is interpreted as the particle's velocity, $A(t)$ represents its position, and the corresponding Feynman-Kac equation coincides with the Klein-Kramers equation[37]. In recent years, efforts have been devoted to extending the Feynman-Kac equations from normal diffusion to anomalous one, with three main approaches: one is to directly introduce temporal memory integral terms into the ordinary Feynman-Kac equations[38]; another one is to adopt the continuous time random walk with specific power-law distributed waiting times[39]; and the last one is to employ the subordination processes. Cairoli et al. first derive the general Feynman-Kac equations using the subordination techniques[40], and further extend the method to the cases involving time- and space-dependent forces as well as time-dependent functionals[41]. To study the positional functionals of polymer particles, Zhou et al. derive Feynman-Kac equations for the polymer model using the subordination method[11,33]. Further, Zhang et al. extend this approach to non-static media and obtain Feynman-Kac equations for polymer model[12]. Wu et al. extend the polymer model to the spherical surface and derive the corresponding Feynman-Kac equations[13].

Benefiting from the powerful high-dimensional representation capability of deep neural networks, a large number of deep learning algorithms for solving high-dimensional complex problems have been proposed. In these algorithms, neural networks serve as basis functions, and loss functions are constructed based on mathematical physics models. The first method is Physics-Informed Neural Networks[16], which constructs the loss function using the L^2 norm of the residual between the two sides of a partial differential equation (PDE). The second one is the deep Ritz method[17], which takes the energy functional of the PDE as the loss function. The third one targets PDEs without an energy functional and achieves equation solving through adversarial learning[18]. The fourth method is the deep Backward Stochastic Differential Equation (BSDE) method[19], which has a stronger machine learning implication and is trained using the sampled trajectories of the stochastic process. Subsequently, Wang et al. extend the deep BSDE method to solve macroscopic equations for polymer center of mass[14], and develop deep learning algorithms for fractional PDEs based on BSDE theory for jump processes[15]. Based on the physical meaning of the solutions and the reflecting boundary conditions, Wang et al. develop a BSDE method for solving high-dimensional PDEs on spheres with reflecting boundary conditions[42].

In this paper, we first characterize the dynamic instability of microtubules by constructing a more refined general polymer model that can describe the non-local polymerization-depolymerization phenomena induced by factors such as kinetochore fibers and katanin proteins. In Section III, based on the established model, we derive the corresponding Fokker-Planck equations and obtain the macroscopic equation for microtubule-kinetochore capture model by imposing appropriate boundary conditions. To study the path functionals of the rotational search of microtubule tips, the derivation of the forward and backward Feynman-Kac equations for the developed model's functionals are presented in Section IV. Since the derived equations are defined in multiple complex domains with dimension higher than three and complex boundary conditions, they cannot be easily solved by using traditional mesh discretization methods. Therefore, we verify the correctness of the mentioned equations by comparing the results obtained from deep BSDE method[14,15,42] and the ones from Monte Carlo simulations in Section V. Finally, we summarize the paper and discuss future prospects.

II. MICROTUBULE GROWTH-ROTATION SEARCH MODEL

A microtubule is a tubular polymer formed by the polymerization of tubulin dimers, which consist of two subunits: α-tubulin and β-tubulin, and its structure is shown in Figure 1(a). The length of a tubulin dimer is approximately 8 nm[7], while the average length of microtubules varies from 1 μm to 50 μm across different cell types[8]. In this paper, microtubules are simplified as linear polymers, and given the constraints of cell volume, we assume that the number of monomers $r(t)$ in such microtubules roughly ranges from $r_{\min}$ to $r_{\max}$. In

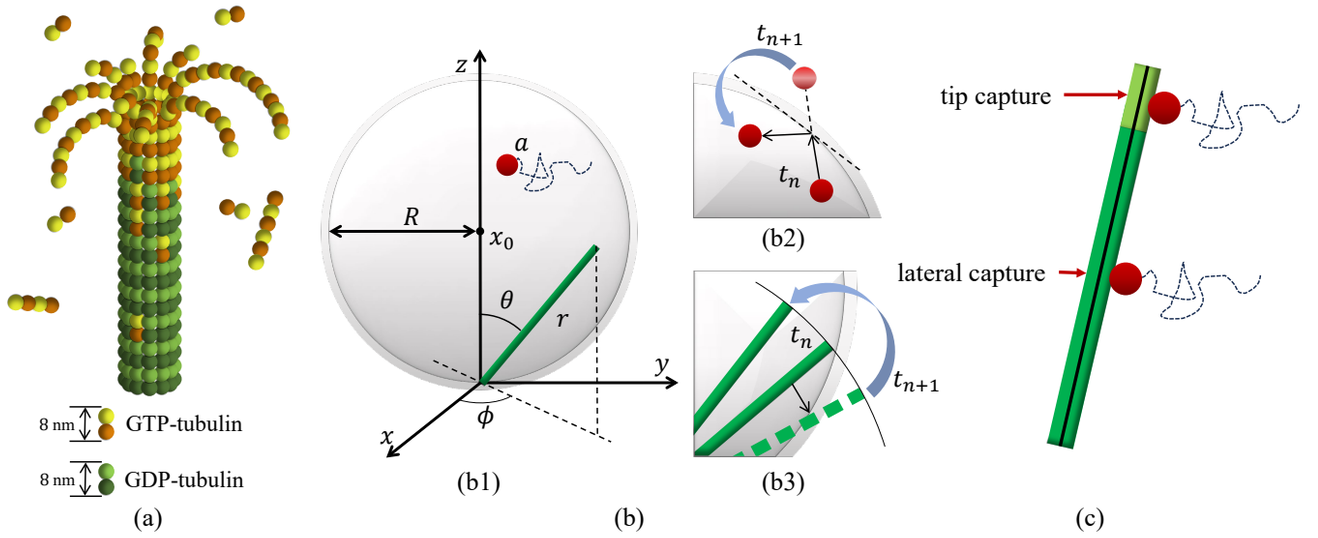

FIG. 1. (a) Schematic diagram of the microtubule structure. A microtubule is a tubular polymer composed of tubulin dimers; each tubulin dimer consists of α-tubulin (light green spheres and light yellow spheres) and β-tubulin (dark green spheres and dark yellow spheres), with a length of approximately 8 nm. (b) Schematic diagram of the positional relationship between microtubules and kinetochores in a cell. We simplify microtubules as linear polymers and establish a Cartesian coordinate system with the centrosome as the origin. Here, θ and ϕ denote the polar angle and azimuthal angle of the microtubule, respectively, and r denotes the length of the microtubule. Kinetochore is treated as a ball with radius a, and when the kinetochore comes into contact with the cell surface, it undergoes specular reflection and rebounds back into the cell (see (b2)). When the microtubule rotates out of the cell, it rebounds back into the cell via specular reflection along the rotation plane (see (b3)). (c) Two modes of kinetochore capture by microtubules. When the kinetochore contacts the tip region of a microtubule (light green), it results in tip capture; when it contacts the lateral region of a microtubule (dark green), it results in lateral capture.

prometaphase, microtubules typically nucleate at the centrosomes and start to grow. As shown in Figure 1(b1), a Cartesian coordinate system is established with the centrosome as the origin and the direction perpendicular to the equatorial plate as the z-axis. In this coordinate system, the polar angle of the microtubule is denoted as $\theta(t)$, and the azimuthal angle is denoted as $\phi(t)$.

To describe the growth-rotation search process of microtubules, we start with the general polymer process $r(t)$, which satisfies $r_{\min} \le r(t) \le r_{\max}$ and the non-local transition probability

$$
\begin{aligned}
&P(r(t+dt)-r(t)=j|r(t)=i)\\
&=\begin{cases}
\lambda_1(i)dt, & j=1,\\
\lambda_2(i)dt, & j=2,\\
\cdots, & \\
\lambda_{r_{\max}-i}(i)dt, & j=(r_{\max}-i),\\
\mu_1(i)dt, & j=-1,\\
\cdots, & \\
\mu_{i-r_{\min}}(i)dt, & j=-(i-r_{\min}),\\
1-\left(\sum\limits_{j=1}^{r_{\max}-i}\lambda_j(i)-\sum\limits_{j=1}^{i-r_{\min}}\mu_j(i)\right)dt, & j=0.
\end{cases}
\end{aligned}
\tag{3}
$$

Here, $\lambda_j(i)$ denotes the rate at which a microtubule of length i polymerizes by a length of j, and $\mu_j(i)$ denotes the rate at which a microtubule of length i depolymerizes by a length of j. Since the length of microtubules exhibits sawtooth-like fluctuating characteristics over time, following a pattern of "growth-stagnation-shortening-regrowth" and that their growth and shortening rates are related to both the current length and the change of length (rather than being constant), we consider using a polymer model. Kinetochore fibers lead to the generation of free non-centrosomal microtubules near chromosomes; these free microtubules can bind to normally growing centrosomal microtubules, thereby promoting the capture of chromosomes[10]. In contrast, the cleavage by katanin protein causes some microtubules to disappear directly[9]. All the aforementioned factors result in non-local polymerization and depolymerization coupling reactions, thus exhibiting non-zero global rates.

Studies have shown that the mean squared angular displacement of the microtubule exhibits a linear relationship with time[5], thus exhibiting characteristics of normal rotation diffusion. To characterize this type of diffusion, we first start with a 3-dimensional Brownian motion

$$
dx(t)=\begin{bmatrix}dx_1(t)\\dx_2(t)\\dx_3(t)\end{bmatrix}=\sqrt{2D_x}\begin{bmatrix}dB_1(t)\\dB_2(t)\\dB_3(t)\end{bmatrix},
\tag{4}
$$

where D_x is the diffusion coefficient and $B_i(t)$, $i=1,2,3$ are independent 1-dimensional Brownian motions satisfying

$$
\mathbb{E}[dB_i(t)]=0,\ dB_i(t)dt=0,\ dB_i(t)dB_j(t)=\begin{cases}dt, & i=j,\\ 0, & i\neq j.\end{cases}
\tag{5}
$$

Let

$$\begin{cases} l(t) = \sqrt{x_1(t)^2 + x_2(t)^2 + x_3(t)^2} \\ \theta(t) = \arccos\left(\dfrac{x_3(t)}{\sqrt{x_1(t)^2 + x_2(t)^2 + x_3(t)^2}}\right), \\ \phi(t) = \arctan\left(\dfrac{x_2(t)}{x_1(t)}\right) \end{cases} \tag{6}$$

be the coordinates of $x(t)$ in the spherical coordinate system. Applying Itô's formula, one can get

$$\begin{cases} dl(t) = \dfrac{2D_x}{l(t)}dt + \sqrt{2D_x}\,(\sin\theta(t)\cos\phi(t)dB_1(t) \\ \qquad + \sin\theta(t)\sin\phi(t)dB_2(t) + \cos\theta(t)dB_3(t)) \\ d\theta(t) = \dfrac{D_x}{l(t)^2}\dfrac{\cos\theta(t)}{\sin\theta(t)}dt + \dfrac{\sqrt{2D_x}}{l(t)}\,(\cos\theta(t)\cos\phi(t)dB_1(t) \\ \qquad + \cos\theta(t)\sin\phi(t)dB_2(t) - \sin\theta(t)dB_3(t)) \\ d\phi(t) = -\dfrac{\sqrt{2D_x}}{l(t)}\left(\dfrac{\sin\phi(t)}{\sin\theta(t)}dB_1(t) + \dfrac{\cos\phi(t)}{\sin\theta(t)}dB_2(t)\right). \end{cases} \tag{7}$$

Combining the general polymer process $r(t)$ with the normal rotational components $\theta(t)$ and $\phi(t)$ of Brownian motion, one can obtain the growth-rotation research model

$$\begin{cases} d\theta(t) = \dfrac{D_x}{r(t)^2}\dfrac{\cos\theta(t)}{\sin\theta(t)}dt + \dfrac{\sqrt{2D_x}}{r(t)}\,(\cos\theta(t)\cos\phi(t)dB_1(t) \\ \qquad + \cos\theta(t)\sin\phi(t)dB_2(t) - \sin\theta(t)dB_3(t)) \\ d\phi(t) = -\dfrac{\sqrt{2D_x}}{r(t)}\left(\dfrac{\sin\phi(t)}{\sin\theta(t)}dB_1(t) + \dfrac{\cos\phi(t)}{\sin\theta(t)}dB_2(t)\right). \end{cases} \tag{8}$$

In practice, the relationship between the growth rate and changes in length may also depend on other physical quantities, and can be obtained through observation and statistical analysis of experimental data. In this paper, we simply assume that the growth rate of microtubules decays exponentially only with the changes in length. However, when the length of a microtubule is relatively large, the GDP-tubulin inside it becomes unstable, thereby making it more prone to defects[1]. This phenomenon causes the shortening rate of microtubules to be related not only to their current length but also to the change in length (with longer microtubules exhibiting a faster shortening rate). In the subsequent simulations of this paper, we set $\lambda_k(r) = c_1 e^{-|k-\bar{k}|}$ and $\mu_k(r) = c_2 r e^{-|k-\bar{k}|}$, where c_1 and c_2 are the intensity parameters for polymerization and depolymerization, respectively, and $\bar{k}$ is the average of microtubule length changes per unit time.

To consider the defect event induced by the cleavage protein, we set $\mu_k(r) = c_2 r e^{-|k-\bar{k}|} + c_3\sqrt{r/\pi}e^{-r|k-(r-r_{\min})|^2}$, where c_3 is the cleavage intensity parameter. As r increases, $\sqrt{r/\pi}e^{-r|k-(r-r_{\min})|^2} \to \delta(k-(r-r_{\min}))$, making defects more likely to occur. Set $c_1 = 36$, $c_2 = 0.2$, $c_3 = 0.02$, $\bar{k} = 10$, $r(0) = r_{\min} = 10$, $r_{\max} = 375$ (3 μm), the time scale is in minutes, and assume that the defect event occurs (the microtubule thus disappears) when $\Delta r(t) = r(t) - r(t-) = r_{\min} - r(t-)$.

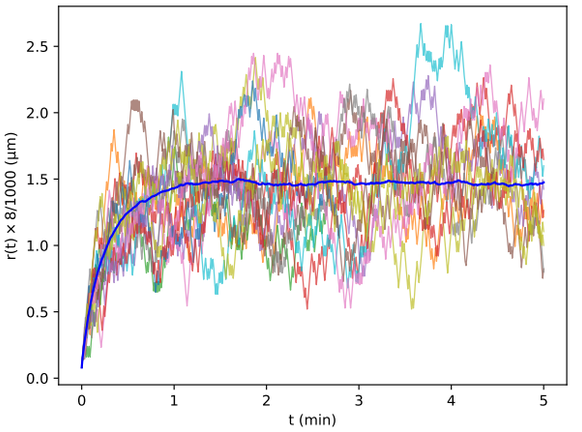

FIG. 2. Microtubule length over time. Here $T = 5$ min, $N = 500$, $c_1 = 36$, $c_2 = 0.2$, $c_3 = 0.02$, $\bar{k} = 10$, $r(0) = r_{\min} = 10$, and $r_{\max} = 375$ (3μm). A change in microtubule length by one unit corresponds to an actual change of 8 nm (8/1000 μm). The ordinate in the figure is converted to units of μm. The colored lines represent the numerical results of Monte Carlo simulations for the lengths of 20 microtubules, and the thick blue line represents the average length of 10^3 microtubules.

We independently simulate the changes of 10^3 microtubule lengths over 5 minutes (see plots of 20 particles in Figure 2). It can be observed from the simulation results that microtubules grow rapidly within the first 0.5 minutes, after which the average length of the microtubules stabilizes at 1.5 μm (see the red line in Figure 2). After 2.5 minutes, the microtubules become sparse, which is consistent with the microtubule length images shown in Figure S2g of reference[5]. In addition, we calculate the average lifespan of the microtubules and obtain a value of approximately 3.0838 minutes, which is consistent with the experimental result of an average microtubule lifetime of 3 minutes[5,7].

III. MICROTUBULE-KINETOCHORE CAPTURE MODEL

Experiments have shown that kinetochores undergo 3-dimensional normal diffusion, and the movement of polar microtubules is not affected by the presence or absence of kinetochores[5]. Thus, the kinetochore can be regarded as a small sphere with radius a (as shown in Figure 1(b-c)), and its movement is characterized by a 3-dimensional Brownian motion $y(t) = \sqrt{2D_y}B_y(t)$ with polar coordinates $(r_y(t), \theta_y(t), \phi_y(t))$. Before the microtubule captures the kinetochore, the two move independently without interfering with each other; after they meet, their movements are no longer independent. Since the movements of both the kinetochore and the microtubule are confined within the cell, the cell is treated as a ball $B(x_0, R)$ with center x_0 and radius $R > r_{\max}/2$. We assume that the centrosome is located at the origin, so the centrosomal microtubules rotate around the ori-

gin. The relative position between the microtubule and the kinetochore is shown in Figure 1(b1). When the kinetochore hits the spherical surface, it is reflected back into the sphere via mirror reflection (see Figure 1(b2)); when the microtubule hits the spherical surface, it is reflected back into the sphere via mirror reflection along the spherical surface of rotation with radius $r(t)$ (see Figure 1(b3)). Defining $x(\theta,\phi) = [\sin\theta\cos\phi, \sin\theta\sin\phi, \cos\theta]^T$, we can give the tip capture conditions (see Figure 1(c))

$$0 \le r(t) - r_y(t)\cos\gamma(t) \le r_{\text{tip}}, \quad r_y(t)\sin\gamma(t) \le a. \tag{9}$$

and the lateral capture conditions

$$0 \le r_y(t)\cos\gamma(t) \le r(t), \quad r_y(t)\sin\gamma(t) \le a, \tag{10}$$

where $\cos\gamma(t) = \frac{x(\theta(t),\phi(t))\cdot y(t)}{|y(t)|}$ ($\gamma(t)$ is the angle between the position vectors of the microtubule and the kinetochore) and r_{tip} is the length of the microtubule tip.

Next, we will derive the Fokker-Planck equations satisfied by the microtubule tip position using the subordination method[11,33], and further obtain the macroscopic dynamic equation for microtubule-kinetochore capture model.

A. Probability density of the functional for the microtubule length

To apply the theory of subordination[11,33], we first consider the integral functional

$$s(t) = \int_0^t \frac{2D_x}{r^2(s)} ds. \tag{11}$$

By applying the property of stationary increment and the left rectangle formula, the increment of the functional within the time interval dt can be obtained as

$$ds(t) = s(t+dt) - s(t) = \frac{2D_x}{r^2(t)} dt. \tag{12}$$

Let $u(r,s,t) = \mathbb{E}\left[\mathbb{I}_{\{r(t)=r\}}\delta(s(t)-s)\right]$ be the joint probability density function of the microtubule length $r(t)$ and the functional $s(t)$ at time t, where $\mathbb{I}$ is the indicator function and $\delta(x)$ is the Dirac function. Then, we have

$$\begin{aligned}
&u(r,s,t+dt)\\
&= \sum_{k=1}^{r_{\max}-r} \mu_k(r+k)u\left(r+k, s-\frac{2D_x}{(r+k)^2}dt, t\right)dt\\
&\quad + \sum_{k=1}^{r-r_{\min}} \lambda_k(r-k)u\left(r-k, s-\frac{2D_x}{(r-k)^2}dt, t\right)dt\\
&\quad + \left(1 - \sum_{k=1}^{r-r_{\min}} \mu_k(r)dt - \sum_{k=1}^{r_{\max}-r} \lambda_k(r)dt\right) u\left(r, s-\frac{2D_x}{r^2}dt, t\right).
\end{aligned} \tag{13}$$

The first term on the right-hand side of (13) represents the contribution to the left-hand side from microtubules with a length of $r+k$ at time t; these microtubules shorten by k length units within the time interval dt with a probability of $\mu_k(r+k)dt$; since the functional at time $t+dt$ is s, according to (12), the functional at time t is $s - \frac{2D_x}{(r+k)^2}dt$. The second term implies the contribution from microtubules with a length of $r-k$ at time t that grow by k length units within dt. The third term indicates the contribution from microtubules with a length of r at time t that neither grow nor shorten within dt.

Doing Fourier transform $s \to p$ on both sides of (13), we have

$$\begin{aligned}
&\tilde{u}(r,p,t+dt)\\
&= \sum_{k=1}^{r_{\max}-r} \mu_k(r+k)e^{-ip\frac{2D_x}{(r+k)^2}dt}\tilde{u}(r+k,p,t)dt\\
&\quad + \sum_{k=1}^{r-r_{\min}} \lambda_k(r-k)e^{-ip\frac{2D_x}{(r-k)^2}dt}\tilde{u}(r-k,p,t)dt\\
&\quad + \left(1 - \sum_{k=1}^{r-r_{\min}} \mu_k(r)dt - \sum_{k=1}^{r_{\max}-r} \lambda_k(r)dt\right) e^{-ip\frac{2D_x}{r^2}dt}\tilde{u}(r,p,t).
\end{aligned}$$

Using the Taylor's expansion of the exponential function, one can get

$$\begin{aligned}
&\tilde{u}(r,p,t+dt)\\
&= \sum_{k=1}^{r_{\max}-r} \mu_k(r+k)\tilde{u}(r+k,p,t)dt + \sum_{k=1}^{r-r_{\min}} \lambda_k(r-k)\tilde{u}(r-k,p,t)dt\\
&\quad + \left(1 - \sum_{k=1}^{r-r_{\min}} \mu_k(r)dt - \sum_{k=1}^{r_{\max}-r} \lambda_k(r)dt\right)\tilde{u}(r,p,t)\\
&\quad - ip\frac{2D_x}{r^2}\tilde{u}(r,p,t)dt.
\end{aligned}$$

Subtracting $\tilde{u}(r,p,t)$ from both sides, dividing by dt, and then performing the inverse Fourier transform $p \to s$, we obtain

$$\frac{\partial}{\partial t}u(r,s,t) = L_r u(r,s,t) - \frac{2D_x}{r^2}\frac{\partial}{\partial s}u(r,s,t), \tag{14}$$

where L_r is the non-local discrete operator on variable r represented as

$$\begin{aligned}
L_r f(r) &= \sum_{k=1}^{r_{\max}-r} \mu_k(r+k)f(r+k) + \sum_{k=1}^{r-r_{\min}} \lambda_k(r-k)f(r-k)\\
&\quad - \left(\sum_{k=1}^{r-r_{\min}} \mu_k(r) + \sum_{k=1}^{r_{\max}-r} \lambda_k(r)\right) f(r).
\end{aligned} \tag{15}$$

Now, considering the conditional probability density

$u_{r_0}(s,t) = \mathbb{E}[\delta(s(t)-s); r(0)=r_0]$, we have

$$\begin{aligned} & u_{r_0}(s,t+dt) \\ &= \sum_{k=1}^{r_{\max}-r_0} \lambda_k(r_0) u_{r_0+k}\left(s - \frac{2D_x}{r_0^2}dt, t\right)dt \\ &+ \sum_{k=1}^{r_0-r_{\min}} \mu_k(r_0) u_{r_0-k}\left(s - \frac{2D_x}{r_0^2}dt, t\right)dt \\ &+ \left(1 - \sum_{k=1}^{r_{\max}-r_0}\lambda_k(r_0)dt - \sum_{k=1}^{r_0-r_{\min}}\mu_k(r_0)dt\right) \\ &\cdot u_{r_0}\left(s - \frac{2D_x}{r_0^2}dt, t\right). \end{aligned} \tag{16}$$

The three terms on the right-hand side of (16) respectively contribute to the left-hand side from the following microtubules: those that start from r_0, grow to r_0+k, shorten to r_0-k, or remain at r_0 within the time interval dt, and then start from r_0+k, r_0-k, or r_0 and reach the functional value s after another time t. After doing the Fourier transform $s \to p$, we obtain

$$\begin{aligned} & \tilde{u}_{r_0}(p,t+dt) \\ &= \sum_{k=1}^{r_{\max}-r_0} \lambda_k(r_0)\tilde{u}_{r_0+k}(p,t)e^{-ip\frac{2D_x}{r_0^2}dt} \\ &+ \sum_{k=1}^{r_0-r_{\min}} \mu_k(r_0)\tilde{u}_{r_0-k}(p,t)e^{-ip\frac{2D_x}{r_0^2}dt} \\ &+ \left(1 - \sum_{k=1}^{r_{\max}-r_0}\lambda_k(r_0)dt - \sum_{k=1}^{r_0-r_{\min}}\mu_k(r_0)dt\right) \\ &\cdot \tilde{u}_{r_0}(p,t)e^{-ip\frac{2D_x}{r_0^2}dt}. \end{aligned}$$

Using the Taylor's expansion of the exponential function, one can obtain

$$\begin{aligned} & \tilde{u}_{r_0}(p,t+dt) \\ &= \sum_{k=1}^{r_{\max}-r_0} \lambda_k(r_0)\tilde{u}_{r_0+k}(p,t)dt + \sum_{k=1}^{r_0-r_{\min}} \mu_k(r_0)\tilde{u}_{r_0-k}(p,t)dt \\ &- \left(\sum_{k=1}^{r_{\max}-r_0}\lambda_k(r_0) + \sum_{k=1}^{r_0-r_{\min}}\mu_k(r_0)\right)\tilde{u}_{r_0}(p,t)dt \\ &+ \left(1 - ip\frac{2D_x}{r_0^2}dt\right)\tilde{u}_{r_0}(p,t). \end{aligned}$$

Subtracting $\tilde{u}_{r_0}(p,t)$ from both sides, dividing by dt, and then performing the inverse Fourier transform $p \to s$, we obtain

$$\frac{\partial}{\partial t}u_{r_0}(s,t) = F_{r_0}u_{r_0}(s,t) - \frac{2D_x}{r_0^2}\frac{\partial}{\partial s}u_{r_0}(s,t), \tag{17}$$

where F_{r_0} is the non-local discrete operator on variable r_0 represented as

$$\begin{aligned} F_{r_0}f_{r_0} = & \sum_{k=1}^{r_{\max}-r_0}\lambda_k(r_0)f_{r_0+k} + \sum_{k=1}^{r_0-r_{\min}}\mu_k(r_0)f_{r_0-k} \\ & - \left(\sum_{k=1}^{r_{\max}-r_0}\lambda_k(r_0) + \sum_{k=1}^{r_0-r_{\min}}\mu_k(r_0)\right)f_{r_0}. \end{aligned} \tag{18}$$

B. Probability density of the microtubule tip position

The subordination method[11,33] transforms a stochastic process $X(t)$ into another stochastic process $Y(t)$ via a time change $Y(t) = X(T(t))$, where $T(t)$ is a subordinator. By applying subordination method, we can rewrite (8) into the subordinated form

$$\begin{cases} d\theta(s) = \dfrac{1}{2}\dfrac{\cos\theta(s)}{\sin\theta(s)}ds + \cos\theta(s)\cos\phi(s)dB_1(s) \\ \qquad + \cos\theta(s)\sin\phi(s)dB_2(s) - \sin\theta(s)dB_3(s), \\ d\phi(s) = -\dfrac{\sin\phi(s)}{\sin\theta(s)}dB_1(s) + \dfrac{\cos\phi(s)}{\sin\theta(s)}dB_2(s), \\ ds(t) = \dfrac{2D_x}{r^2(t)}dt. \end{cases} \tag{19}$$

To go further, let us consider the joint probability density function $u(\theta,\phi,s) = \mathbb{E}[\delta(\theta-\theta(s))\delta(\phi-\phi(s)); s(t)=s]$, which is a L^2-integrable function on the sphere. Therefore, it is necessary to derive the governing equation via the Fourier transform in the spherical coordinate system[43]. The Fourier transform of $u(\theta,\phi,s)$ in the spherical coordinate system $(\theta \to l, \phi \to m)$ is

$$\begin{aligned} \tilde{u}(l,m,s) =& \mathscr{F}_{l,m}\{u(\theta,\phi,s)\} \\ =& \int_0^{2\pi}\int_0^{\pi} u(\theta,\phi,s)Y_{lm}^*(\theta,\phi)\sin\theta d\theta d\phi \\ =& \mathbb{E}[Y_{lm}^*(\theta(s),\phi(s))\sin\theta(s)], \end{aligned} \tag{20}$$

where $Y_{lm}^*(\theta,\phi)$ are the spherical harmonics (see Appendix A for more detailed introduction). Using Taylor's expansion and the properties of Brownian motion in (5), one can get (see Appendix B)

$$\begin{aligned} & \tilde{u}(l,m,s+ds) - \tilde{u}(l,m,s) \\ =& \frac{1}{2}\mathscr{F}_{l,m}\left\{\frac{1}{\sin^2\theta}u(\theta,\phi,s) - \frac{\cos\theta}{\sin\theta}\frac{\partial}{\partial\theta}u(\theta,\phi,s)\right. \\ &\left. + \frac{\partial}{\partial\theta^2}u(\theta,\phi,s) + \frac{1}{\sin^2\theta}\frac{\partial}{\partial\phi^2}u(\theta,\phi,s)\right\}ds. \end{aligned} \tag{21}$$

Dividing both sides by ds, and performing the inverse Fourier transform, one can get

$$\frac{\partial}{\partial s}u(\theta,\phi,s) = \frac{1}{2}\tilde{\Delta}_S u(\theta,\phi,s), \tag{22}$$

where the operator $\tilde{\Delta}_S$ is defined as

$$\begin{aligned} \tilde{\Delta}_S f(\theta,\phi) =& \frac{1}{\sin^2\theta}f(\theta,\phi) - \frac{\cos\theta}{\sin\theta}\frac{\partial}{\partial\theta}f(\theta,\phi) \\ &+ \frac{\partial^2}{\partial\theta^2}f(\theta,\phi) + \frac{1}{\sin^2\theta}\frac{\partial^2}{\partial\phi^2}f(\theta,\phi). \end{aligned} \tag{23}$$

Now, one can get the joint probability density $u(r,\theta,\phi,t) = \mathbb{E}\left[\mathbb{I}_{\{r(t)=r\}}\delta(\theta(t)-\theta)\delta(\phi(t)-\phi)\right]$ by averaging over s in the form

$$u(r,\theta,\phi,t) = \int_0^{\infty} u(r,s,t)u(\theta,\phi,s)ds. \tag{24}$$

Equation (24) is the well-known subordination formula[11,33]. Then, by differentiating both sides of (24) with respect to t and combining it with (14) and (22), one can obtain the Fokker-Planck equation

$$\begin{aligned}
&\frac{\partial}{\partial t}u(r,\theta,\phi,t)\\
=&\int_0^\infty \frac{\partial}{\partial t}u(r,s,t)u(\theta,\phi,s)ds\\
=&L_r u(r,\theta,\phi,t)-\frac{2D_x}{r^2}\int_0^\infty u(\theta,\phi,s)\frac{\partial}{\partial s}u(r,s,t)ds\\
=&L_r u(r,\theta,\phi,t)+\frac{2D_x}{r^2}\int_0^\infty \frac{\partial}{\partial s}u(\theta,\phi,s)u(r,s,t)ds\\
=&L_r u(r,\theta,\phi,t)+\frac{D_x}{r^2}\tilde{\Delta}_S u(r,\theta,\phi,t).
\end{aligned} \tag{25}$$

Similarly, one can get the conditional joint probability density $u_{r_0}(\theta,\phi,t)=\mathbb{E}[\delta(\theta(t)-\theta)\delta(\phi(t)-\phi);r(0)=r_0]$ by

$$u_{r_0}(\theta,\phi,t)=\int_0^\infty u_{r_0}(s,t)u(\theta,\phi,s)ds,$$

as well as the corresponding governing equation

$$\frac{\partial}{\partial t}u_{r_0}(\theta,\phi,t)=F_{r_0}u_{r_0}(\theta,\phi,t)+\frac{D_x}{r_0^2}\tilde{\Delta}_S u_{r_0}(\theta,\phi,t). \tag{26}$$

C. Macroscopic equation for microtubule-kinetochore capture model

The probability density of the position for the kinetochore $p(y,t)=\mathbb{E}[\delta(y(t)-y)]$ satisfies the diffusion equation

$$\frac{\partial}{\partial t}p(y,t)=D_y\nabla_y^2 p(y,t). \tag{27}$$

Before considering the capture event between the microtubule and the kinetochore, let us first consider the case where they are independent of each other. Denoting $u(r,\theta,\phi,y,t)=\mathbb{E}\left[\mathbb{I}_{\{r(t)=r\}}\delta(\theta(t)-\theta)\delta(\phi(t)-\phi)\delta(y(t)-y)\right]$ as the joint probability density of the microtubule tip position and the kinetochore position, we can obtain

$$u(r,\theta,\phi,y,t)=u(r,\theta,\phi,t)p(y,t). \tag{28}$$

By differentiating both sides of (28) with respect to t and combining it with (25) and (27), one can get

$$\begin{aligned}
&\frac{\partial}{\partial t}u(r,\theta,\phi,y,t)\\
=&\frac{\partial}{\partial t}u(r,\theta,\phi,t)p(y,t)+u(r,\theta,\phi,t)\frac{\partial}{\partial t}p(y,t)\\
=&L_r u(r,\theta,\phi,t)p(y,t)+\frac{D_x}{r^2}\tilde{\Delta}_S u(r,\theta,\phi,t)p(y,t)\\
&+u(r,\theta,\phi,t)D_y\nabla_y^2 p(y,t)\\
=&L_r u(r,\theta,\phi,y,t)+\frac{D_x}{r^2}\tilde{\Delta}_S u(r,\theta,\phi,y,t)+D_y\nabla_y^2 u(r,\theta,\phi,y,t).
\end{aligned} \tag{29}$$

After a microtubule successfully captures a kinetochore, their movements are no longer independent, so they "disappear" from (29). Therefore, by adding the absorbing boundary conditions

$$u(r,\theta,\phi,y,t)=0,\quad 0\le r-|y|\cos\gamma\le r_{\text{tip}},\quad |y|\sin\gamma\le a, \tag{30}$$

for tip capture or

$$u(r,\theta,\phi,y,t)=0,\quad 0\le |y|\cos\gamma\le r,\quad |y|\sin\gamma\le a, \tag{31}$$

for lateral capture with $\gamma=\arccos\left(\frac{x(\theta,\phi)\cdot y}{|y|}\right)$, the physical meaning of the solution for (29) becomes to the survival probability density of microtubules and kinetochores without capture events. To ensure that microtubule and kinetochore always move within the cell, we also need to impose appropriate reflecting boundary conditions on the macroscopic equations. For kinetochore, one can directly impose a reflecting boundary condition

$$\left.\frac{\partial u}{\partial n_y}\right|_{|y-x_0|=R}=0. \tag{32}$$

When the length of the microtubule is $r\times 8/1000$ μm, it comes into contact with $\partial B(x_0,R)$ when the polar angle satisfies $\theta=\arccos\left(\frac{r\times 8/1000}{2R}\right)$; thus, we should apply a reflecting boundary condition

$$\left.\left(\frac{\partial u}{\partial\theta}-\frac{\cos\theta}{\sin\theta}u\right)\right|_{\theta=\arccos\left(\frac{r\times 8/1000}{2R}\right)}=0. \tag{33}$$

Additionally, u is subject to an absorbing boundary condition

$$u|_{\theta=0}=0 \tag{34}$$

and a periodic boundary condition

$$u|_{\phi=0}=u|_{\phi=2\pi}. \tag{35}$$

Now, one can calculate the survival probability by

$$P(t)=\int_{\mathbb{R}^3}\int_0^{2\pi}\sum_{r=r_{\min}}^{r_{\max}}\int_0^{\arccos\left(\frac{r\times 8/1000}{2R}\right)}u(r,\theta,\phi,y,t)d\theta d\phi dy \tag{36}$$

and get the capture probability by $G(t)=1-P(t)$.

IV. DERIVATION OF THE FEYNMAN-KAC EQUATION

The functionals of stochastic process have numerous applications[44,45] and widely appear in various problems across multiple scientific fields, including condensed matter physics[46–48], hydrodynamics[49], meteorology[50], and finance[51]. Consider the integral functional for the tip position of the growth-rotation microtubule represented as

$$A(t)=\int_0^t U(r(s)x(\theta(s),\phi(s)))ds, \tag{37}$$

where $U(x) \in \mathbb{R}$ is a given function. We first consider the joint probability density function $u(r,\theta,\phi,A,t) = \mathbb{E}\left[\mathbb{I}_{\{r(t)=r\}}\delta(\theta(t)-\theta)\delta(\phi(t)-\phi)\delta(A(t)-A)\right]$. Performing Fourier transform $\theta \to l$, $\phi \to m$, $A \to p$, we have

$$\tilde{u}(r,l,m,p,t) = \mathbb{E}\left[\mathbb{I}_{\{r(t)=r\}} e^{-ipA(t)} Y_{lm}^*(\theta(t),\phi(t))\sin\theta(t)\right]. \tag{38}$$

Using the definition (3), Taylor's expansion, and the properties of Brownian motion in (5), one can get (see Appendix C)

$$\begin{aligned}&\tilde{u}(r,l,m,p,t+dt) - \tilde{u}(r,l,m,p,t)\\ =&L_r\tilde{u}(r,l,m,p,t)dt + \mathscr{F}_{l,m}\left\{\frac{D_x}{r^2}\tilde{\Delta}_S\tilde{u}(r,\theta,\phi,p,t)\right.\\ &\left. - ipU(rx(\theta,\phi))\tilde{u}(r,\theta,\phi,p,t)\right\}dt.\end{aligned} \tag{39}$$

Dividing both sides by dt, and performing the inverse Fourier transform, we obtain the forward Feynman-Kac equation

$$\begin{aligned}\frac{\partial}{\partial t}\tilde{u}(r,\theta,\phi,p,t) =&L_r\tilde{u}(r,\theta,\phi,p,t) + \frac{D_x}{r^2}\tilde{\Delta}_S\tilde{u}(r,\theta,\phi,p,t)\\ &- ipU(rx(\theta,\phi))\tilde{u}(r,\theta,\phi,p,t).\end{aligned} \tag{40}$$

Since in applications, sometimes only the equation satisfied by the probability density function of the position functional is interested in, rather than the joint distribution of the position and functional, we take the initial position coordinates $r(0) = r_0$, $\theta(0) = \theta_0$, $\phi(0) = \phi_0$ as known conditions and consider the position functional

$$A_{r_0,\theta_0,\phi_0}(t) = \int_0^t U(r|_{r_0}(s)x(\theta|_{\theta_0}(s),\phi|_{\phi_0}(s)))ds, \tag{41}$$

as well as its probability density function $u_{r_0,\theta_0,\phi_0}(A,t) = \mathbb{E}\left[\delta(A|_{r_0,\theta_0,\phi_0}(t)-A)\right]$, where $r|_{r_0}(t)$, $\theta|_{\theta_0}(t)$, and $\phi|_{\phi_0}(t)$ are the tip positions $r(t)$, $\theta(t)$, $\phi(t)$ of the microtubule at time t with $r(0) = r_0$, $\theta(0) = \theta_0$, $\phi(0) = \phi_0$, respectively. Performing Fourier transform $A \to p$, we have

$$\tilde{u}_{r_0,\theta_0,\phi_0}(p,t) = \mathbb{E}\left[e^{-ipA_{r_0,\theta_0,\phi_0}(t)}\right]. \tag{42}$$

Using the definition (41), Taylor's expansion, and the double expectation formula, one can get

$$\begin{aligned}&\tilde{u}_{r_0,\theta_0,\phi_0}(p,t+dt) - \tilde{u}_{r_0,\theta_0,\phi_0}(p,t)\\ =&\mathbb{E}\left[e^{-ipA|_{r_0,\theta_0,\phi_0}(t+dt)}\right] - \mathbb{E}\left[e^{-ipA|_{r_0,\theta_0,\phi_0}(t)}\right]\\ =&\mathbb{E}\left[e^{-ip\left(U(r_0x(\theta_0,\phi_0))dt + A|_{r|_{r_0}(dt),\theta|_{\theta_0}(dt),\phi|_{\phi_0}(t)}(t)\right)}\right]\\ &- \mathbb{E}\left[e^{-ipA|_{r_0,\theta_0,\phi_0}(t)}\right]\\ =&\mathbb{E}\left[e^{-ipA|_{r|_{r_0}(dt),\theta|_{\theta_0}(dt),\phi|_{\phi_0}(dt)}(t)}\right] - \mathbb{E}\left[e^{-ipA|_{r_0,\theta_0,\phi_0}(t)}\right]\\ &- ipU(r_0x(\theta_0,\phi_0))\mathbb{E}\left[e^{-ipA|_{r_0,\theta_0,\phi_0}(t)}\right]dt\\ =&\mathbb{E}\left[\tilde{u}_{r|_{r_0}(dt),\theta|_{\theta_0}(dt),\phi|_{\phi_0}(t)}(p,t)\right] - \tilde{u}_{r_0,\theta_0,\phi_0}(p,t)\\ &- ipU(r_0x(\theta_0,\phi_0))\tilde{u}_{r_0,\theta_0,\phi_0}(p,t)dt.\end{aligned} \tag{43}$$

Then, one can use the definition (3), Taylor's expansion, and the properties of the Brownian motion in (5) to get (see Appendix D)

$$\begin{aligned}&\mathbb{E}\left[\tilde{u}_{r|_{r_0}(dt),\theta|_{\theta_0}(dt),\phi|_{\phi_0}(dt)}(p,t)\right] - \tilde{u}_{r_0,\theta_0,\phi_0}(p,t)\\ =&F_{r_0}\tilde{u}_{r_0,\theta_0,\phi_0}(p,t)dt + \frac{D_x}{r_0^2}\Delta_S\tilde{u}_{r_0,\theta_0,\phi_0}(p,t)dt,\end{aligned} \tag{44}$$

where the operator Δ_S is defined as

$$\begin{aligned}\Delta_S f(\theta,\phi) =&\frac{1}{\sin\theta}\frac{\partial}{\partial\theta}\left(\sin\theta\frac{\partial}{\partial\theta}f(\theta,\phi)\right)\\ &+\frac{1}{\sin^2\theta}\frac{\partial^2}{\partial\phi^2}f(\theta,\phi).\end{aligned} \tag{45}$$

Substituting (44) into (43) and dividing both sides of (43) by dt, one can get the backward Feynman-Kac equation

$$\begin{aligned}\frac{\partial}{\partial t}\tilde{u}_{r_0,\theta_0,\phi_0}(p,t) =&F_{r_0}\tilde{u}_{r_0,\theta_0,\phi_0}(p,t) + \frac{D_x}{r_0^2}\Delta_S\tilde{u}_{r_0,\theta_0,\phi_0}(p,t)\\ &- ipU(r_0x(\theta_0,\phi_0))\tilde{u}_{r_0,\theta_0,\phi_0}(p,t).\end{aligned} \tag{46}$$

V. APPLICATIONS

The deep BSDE method[14,15,19] is a deep learning algorithm for solving high-dimensional PDEs in the whole domain. In essence, it transforms the problem of solving PDEs into solving the corresponding BSDEs that share the same solution as the PDEs. By constructing appropriate stochastic processes, Wang et al. extend this method to solve high-dimensional coupled PDEs on manifold with reflecting and absorbing boundaries[14,42]. In this section, we focus on several applications, including the probability density of the growth-rotation model, microtubule-kinetochore capture, occupation time, and the joint probability density of position and integral functional. By comparing the results obtained from the deep learning algorithm[14,42] and the Monte Carlo method across these applications, we verify the reasonableness of the equations derived in Sections III and IV. All numerical experiments are performed on a personal computer equipped with an NVIDIA GeForce RTX 4070 Ti GPU with 64 GB of system memory and 12 GB of GPU memory. We open the source code for readers to test: `https://github.com/WANGH950/MKCapture`.

A. Probability density of the growth-rotation model

We first consider the Fokker-Planck equation for the growrotation model, expressed as

$$\frac{\partial}{\partial t}u(r,\theta,\phi,t) = L_r u(r,\theta,\phi,t) + \frac{D_x}{r^2}\tilde{\Delta}_S u(r,\theta,\phi,t) \tag{47}$$

with reflecting boundary condition

$$\left(\frac{\partial u}{\partial\theta} - \frac{\cos\theta}{\sin\theta}u\right)\Big|_{\theta=\arccos\left(\frac{r\times 8/1000}{2R}\right)} = 0. \tag{48}$$

To apply the deep learning method[14,42], we denote $p(r,x(\theta,\phi),t)$ as the joint probability density of $r(t)$ and $x(\theta(t),\phi(t))$ at time t, and use the relationship $u(r,\theta,\phi,t) = p(r,x(\theta,\phi),t)\sin\theta$ to transform (47) and (48) as

$$\frac{\partial}{\partial t}p(r,x(\theta,\phi),t) = L_r p(r,x(\theta,\phi),t) + \frac{D_x}{r^2}\Delta_S p(r,x(\theta,\phi),t) \tag{49}$$

and

$$\nabla_x p \cdot \frac{\partial x}{\partial \theta}\bigg|_{\theta=\arccos\left(\frac{r\times 8/1000}{2R}\right)} = 0.$$

Performing a time transformation $t \to T - t$ on (49), we choose $T = 1$, $D_x = 10$, $c_1 = 1$, $c_2 = 0.1$, $\bar{k} = 2$, $r_{\min} = 5$, $r_{\max} = 50$, $R = 2$, and the terminal condition (initial condition before the time transformation)

$$p(r,x(\theta,\phi),T) = \begin{cases} \dfrac{1}{\sin\theta}, & \theta_b(r) - \dfrac{\pi}{4} < \theta < \theta_b(r), \\ 0, & \text{otherwise}, \end{cases}$$

where $\theta_b(r) = \arccos\left(\frac{r\times 8/1000}{2R}\right)$. Figure 3 plots the top views of the solution $p(r=10,x(\theta,\phi),t=0)$ to (49) (with respect to x) obtained via the deep learning algorithm and the Monte Carlo algorithm at $r = 10$ and $t = 0$, as well as the absolute error between these two results. We choose the number of time discretization steps as 10^2 ($N = 10^2$), the depth and width of the subnetworks are 3 and $64 + d_{\text{out}}$ (where d_{out} denotes the output dimension of the corresponding subnetwork), the tensor parameter $P = 256$, and the number of samples $M = 10^4$ (which is used for approximating integrals). The deep learning result is obtained after 10^4 iteration steps with a learning rate of 5×10^{-4} and a batch size of 512. The Monte Carlo simulation result is obtained by approximately calculating the probability density with 10^8 independent particle trajectories. The simulation results show that the results obtained by directly solving (49) match those from Monte Carlo simulations, illustrating the reasonableness of the derived equation.

B. Microtubule-Kinetochore capture

We consider the macroscopic equation (29) for microtubule-kinetochore capture model. Defining $p(r,x(\theta,\phi),y,t)$ as the joint probability density of $r(t)$, $x(\theta(t),\phi(t))$, and $y(t)$ at time t, and using the relationship $u(r,\theta,\phi,y,t) = p(r,x(\theta,\phi),y,t)\sin\theta$, one can get

$$\begin{aligned} &\frac{\partial}{\partial t}p(r,x(\theta,\phi),y,t) \\ =&L_r p(r,x(\theta,\phi),y,t) + \frac{D_x}{r^2}\Delta_S p(r,x(\theta,\phi),y,t) \\ &+ D_y\nabla_y^2 p(r,x(\theta,\phi),y,t) \end{aligned} \tag{50}$$

with reflecting boundary conditions

$$\nabla_x p \cdot \frac{\partial x}{\partial \theta}\bigg|_{\theta=\arccos\left(\frac{r\times 8/1000}{2R}\right)} = 0, \quad \nabla_y p\big|_{|y-x_0|=R} = 0,$$

and absorbing boundary condition

$$p(r,x(\theta,\phi),y,t) = 0$$

for $0 \le r - |y|\cos\gamma \le r_{\text{tip}}$, and $|y|\sin\gamma \le a$.

Performing a time transformation $t \to T - t$ on (50), we choose $T = 0.1$, $D_x = 50$, $D_y = 1$, $a = 0.05$, $r_{\text{tip}} = 0.05$, $c_1 = 5$, $c_2 = 0.1$, $\bar{k} = 4$, $r_{\min} = 10$, $r_{\max} = 100$, $R = 0.5$, and the terminal condition

$$\begin{aligned} &p(r,x(\theta,\phi),y,T) \\ =&\mathbb{I}_{\{\theta<\theta_b(r),r\le 50,y_3>R\}} \Big/ \left(1 - \frac{r\times 8/1000}{2R}\right) \end{aligned}$$

with $\theta_b(r) = \arccos\left(\frac{r\times 8/1000}{2R}\right)$. Focusing on the solution $p(r,x(\theta,\phi),y,0)$ at fixed point ($r = 40, x(\theta,\phi) = [0,0,1]^T, y = [0,0,0.6]$), Figure 4 shows the variation of the deep learning results with the number of iterations (blue solid line), as well as the "exact solution" obtained from Monte Carlo simulations (red solid line). We choose the number of time discretization steps as 10^2 ($N = 10^2$), the depth and width of the subnetworks are 4 and $64 + d_{\text{out}}$, the tensor parameter $P = 128$, and the number of samples $M = 10^4$. The deep learning result is obtained after 10^4 iteration steps with a learning rate of 5×10^{-4} and a batch size of 512. The Monte Carlo simulation result is obtained by approximately calculating the probability density with 10^9 independent particle trajectories. The agreement between the two simulation results confirms the correctness of (50).

C. Occupation time

In this subsection, we consider the backward Feynman-Kac equation

$$\begin{aligned} \frac{\partial}{\partial t}\tilde{u}_{r_0,\theta_0,\phi_0}(p,t) =& F_{r_0}\tilde{u}_{r_0,\theta_0,\phi_0}(p,t) + \frac{D_x}{r_0^2}\Delta_S\tilde{u}_{r_0,\theta_0,\phi_0}(p,t) \\ &- ipU(r_0x(\theta_0,\phi_0))\tilde{u}_{r_0,\theta_0,\phi_0}(p,t) \end{aligned} \tag{51}$$

with the initial condition

$$\begin{aligned} \tilde{u}_{r_0,\theta_0,\phi_0}(p,0) =& \mathscr{F}_p\{u_{r_0,\theta_0,\phi_0}(A,0)\} \\ =& \mathscr{F}_p\{\delta(A)\} = 1 \end{aligned}$$

and the reflecting boundary condition

$$\frac{\partial\tilde{u}_{r_0,\theta_0,\phi_0}}{\partial\theta_0}\bigg|_{\theta_0=\arccos\left(\frac{r_0\times 8/1000}{2R}\right)} = 0. \tag{52}$$

We denote $p_{r_0,x(\theta_0,\phi_0)}(A,t)$ as the probability density function of $A(t)$ at time t with the conditions $r(0) = r_0$ and $x(\theta(0),\phi(0)) = x(\theta_0,\phi_0)$. Since (θ_0,ϕ_0) and $x(\theta_0,\phi_0)$ represent the same condition point, $p_{r_0,x(\theta_0,\phi_0)} = u_{r_0,x(\theta_0,\phi_0)}$ and $p_{r_0,x(\theta_0,\phi_0)}$ satisfies (51) with the reflecting boundary condition

$$\nabla_x\tilde{p}_{r_0,x(\theta_0,\phi_0)} \cdot \frac{\partial x}{\partial\theta_0}\bigg|_{\theta_0=\arccos\left(\frac{r_0\times 8/1000}{2R}\right)} = 0. \tag{53}$$

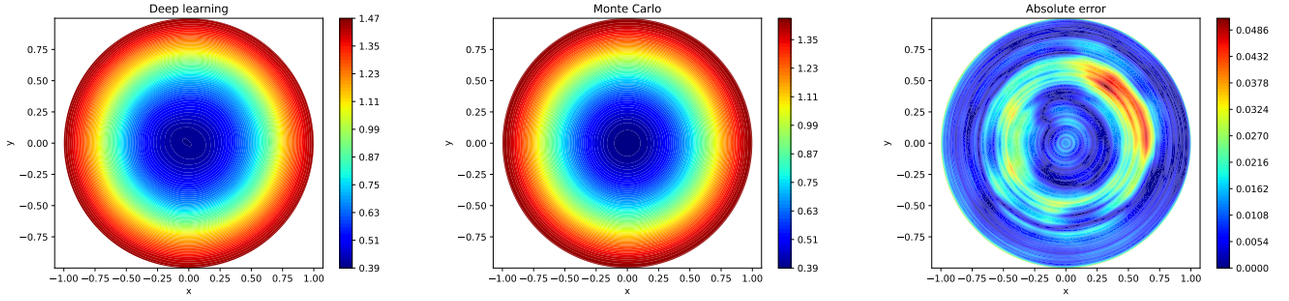

(a) (b) (c)

FIG. 3. Plots of the solutions to (49) obtained by the deep learning method[14,42] and the Monte Carlo simulation as well as the absolute error between these results. (a) Plot of the top view for the solution to the diffusion equation (49), which is obtained by the deep learning method trained in 10^4 iteration steps with a learning rate of 5×10^{-4}. (b-c) Plots of the "exact solution" (obtained by approximately calculating the probability density with 10^8 particle trajectories simulated by the Monte Carlo method) and the absolute error relative to the deep learning result.

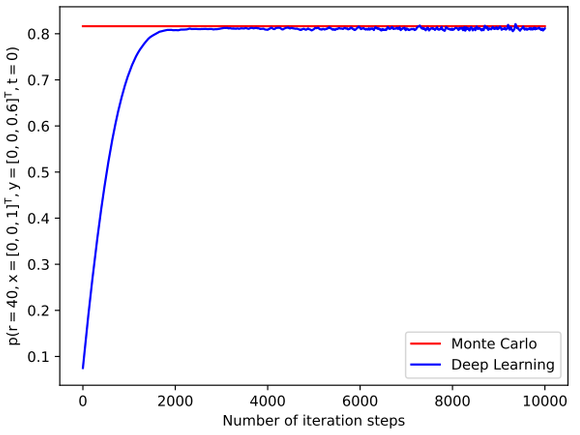

FIG. 4. Plot of the convergence of the deep learning result, where the blue solid line represents the solutions $p(r=40,x=[0,0,1]^T,y=[0,0,0.6]^T,0)$ to (50) at $r=40$, $x=[0,0,1]^T$, $y=[0,0,0.6]^T$, and $t=0$, which is obtained by the deep learning method[14,42]. The red straight line represent the "exact solution" obtained by the Monte Carlo method. We choose the number of time discretization steps as 10^2 ($N=10^2$), the depth and width of the subnetworks are 4 and $64+d_{\text{out}}$, the tensor parameter $P=128$, and the number of samples $M=10^4$. The deep learning results are obtained after 10^4 iteration steps with a learning rate of 5×10^{-4} and a batch size of 512. The Monte Carlo simulation results are obtained by approximately calculating the probability density with 10^9 independent particle trajectories with 10^2 time steps ($N=10^2$).

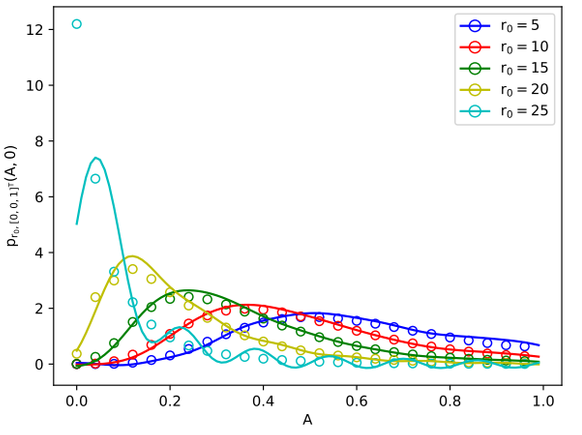

FIG. 5. Plots of the solutions $p_{r_0,x(\theta_0,\phi_0)=[0,0,1]^T}(A,0)$ to (51) at $r_0=5$, 10, 15, 20, and 25 (solid lines), which are obtained by performing the inverse Fourier transform on the deep learning results[14,42]. It also plots the approximate probability densities of the functional derived from particle trajectory simulations via the Monte Carlo method (open circles). We choose the number of time discretization steps as 10^2 ($N=10^2$), the depth and width of the subnetworks are 4 and $64+d_{\text{out}}$, the tensor parameter $P=128$, and the number of samples $M=10^4$. The deep learning results are obtained after 10^4 iteration steps with a learning rate of 5×10^{-4} and a batch size of 512. The Monte Carlo simulation results are obtained by approximately calculating the probability density with 10^7 independent particle trajectories for each r_0 with 10^3 time steps ($N=10^3$).

One application of the Feynman-Kac equation is to solve the occupation time of a particle's position within a region of interest. Here, we consider the occupation time of the microtubule tip position in the region $x_3<c$; thus, we define

$$U(rx(\theta,\phi))=\begin{cases}1, & rx_3(\theta,\phi)\times 8/1000\le c,\\ 0, & \text{otherwise.}\end{cases} \tag{54}$$

Performing a time transformation $t\to T-t$ on (51), we choose $T=1$, $D_x=5$, $c=0.2$ $c_1=10$, $c_2=0.1$, $\bar{k}=2$, $r_{\min}=5$, $r_{\max}=100$, and $R=2$. Figure 5 plots the solutions $p_{r_0,x(\theta_0,\phi_0)=[0,0,1]^T}(A,0)$ to (51) at $r_0=5$, 10, 15, 20, and 25 via deep learning method[14,42] (solid lines), as well as the approximate probabilities densities of the functional calculated via particle trajectory simulations using the Monte Carlo

method (open circles). We choose the number of time discretization steps as 10^2 ($N = 10^2$), the depth and width of the subnetworks are 4 and $64+d_{\text{out}}$, the tensor parameter $P = 128$, and the number of samples $M = 10^4$. Furthermore, we truncate the frequency to a finite interval $[-40, 40]$, and obtain the results in the time domain via the inverse numerical Fourier transform. The deep learning results are obtained after 10^4 iteration steps with a learning rate of 5×10^{-4} and a batch size of 512. The Monte Carlo simulation results are obtained by approximately calculating the probability density with 10^7 independent particle trajectories for each r_0 with 10^3 time steps ($N = 10^3$). The results show that the peak of the occupation time distribution of the microtubule tip in the region $x_3 \leq 0.2$ decreases as the initial length r_0 increases. It is displayed that the deep learning results match the Monte Carlo ones, and thus the correctness of the backward Feynman-Kac equation (51) is verified.

D. Joint distribution of position and integral functional

Let us now consider the forward Feynman-Kac equation of the microtubule growth-rotation model

$$\begin{aligned}\frac{\partial}{\partial t}\tilde{u}(r,\theta,\phi,p,t) =& L_r\tilde{u}(r,\theta,\phi,p,t) + \frac{D_x}{r^2}\tilde{\Delta}_S\tilde{u}(r,\theta,\phi,p,t)\\ &- ipU(rx(\theta,\phi))\tilde{u}(r,\theta,\phi,p,t)\end{aligned} \tag{55}$$

with the initial condition

$$\begin{aligned}\tilde{u}(r,\theta,\phi,p,0) =& \mathscr{F}_p\{u_0(r,\theta,\phi,A)\}\\ =& \mathscr{F}_p\{u_0(r,\theta,\phi)\delta(A)\}\\ =& u_0(r,\theta,\phi)\end{aligned}$$

and the reflecting boundary condition

$$\left.\frac{\partial\tilde{u}}{\partial\theta} - \frac{\cos\theta}{\sin\theta}\tilde{u}\right|_{\theta=\arccos\left(\frac{r\times 8/1000}{2R}\right)} = 0. \tag{56}$$

We denote $p(r,x(\theta,\phi),A,t)$ as the joint probability density of $r(t)$, $x(\theta(t),\phi(t))$, $A(t)$ at time t. Using the relationship $u(r,\theta,\phi,A,t) = p(r,x(\theta,\phi),A,t)\sin\theta$, one can get

$$\begin{aligned}&\frac{\partial}{\partial t}\tilde{p}(r,x(\theta,\phi),p,t)\\ =& L_r\tilde{p}(r,x(\theta,\phi),p,t) + \frac{D_x}{r^2}\Delta_S\tilde{p}(r,x(\theta,\phi),p,t)\\ &- ipU(rx(\theta,\phi))\tilde{p}(r,x(\theta,\phi),p,t),\end{aligned} \tag{57}$$

and the reflecting boundary condition (56) becomes to

$$\nabla\tilde{p}\cdot\left.\frac{\partial x}{\partial\theta}\right|_{\theta=\arccos\left(\frac{r\times 8/1000}{2R}\right)} = 0.$$

In this application, we also consider the functional about the occupation time, which is defined as (54). Performing a time transformation $t \to T - t$ on (57), we choose $T = 1$, $D_x = 50$, $c = 0.15$, $c_1 = 10$, $c_2 = 0.1$, $\bar{k} = 2$, $r_{\min} = 5$, $r_{\max} = 100$, $R = 2$, and the terminal condition

$$p(r,x(\theta,\phi),T) = \begin{cases}\dfrac{1}{\sin\theta}, & \theta_b(r) - \dfrac{3\pi}{8} < \theta < \theta_b(r), r \leq 10,\\ 0, & \text{otherwise.}\end{cases}$$

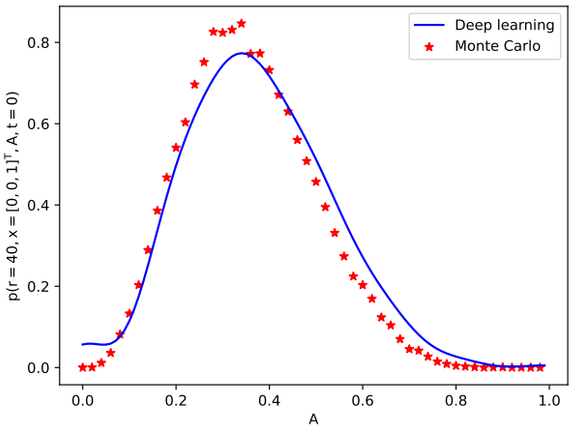

FIG. 6. Plots of the solutions $p(r = 40, x(\theta,\phi) = [0,0,1]^T, A, t = 0)$ to (57) at $r = 40$ and $x(\theta,\phi) = [0,0,1]^T$ obtained by performing the inverse Fourier transform on the deep learning results[14,42] (solid line), and the approximate joint probability densities of the functional derived from particle trajectory simulations via the Monte Carlo method (open circles). We choose the number of time discretization steps as 10^2 ($N = 10^2$), the depth and width of the subnetworks are 4 and $64+d_{\text{out}}$, the tensor parameter $P = 128$, and the number of samples $M = 10^4$. The deep learning results are obtained after 10^4 iteration steps with a learning rate of 5×10^{-4} and a batch size of 512. The Monte Carlo simulation results are obtained by approximately calculating the probability density with 10^9 independent particle trajectories with 10^2 time steps ($N = 10^2$).

Figure 6 shows the solution $p(r = 40, x(\theta,\phi) = [0,0,1]^T, A, t = 0)$, as well as the approximate joint probability density of the tip position and the functional calculated via Monte Carlo method. We choose the number of time discretization steps as 10^2 ($N = 10^2$), the depth and width of the subnetworks are 4 and $64+d_{\text{out}}$, the tensor parameter $P = 128$, and the number of samples $M = 10^4$. The deep learning result is obtained after 10^4 iteration steps with a learning rate of 5×10^{-4} and a batch size of 512. The Monte Carlo simulation result is obtained by approximately calculating the probability density with 10^9 independent particle trajectories. The agreement between the two simulation results verifies the correctness of (54).

VI. CONCLUSION

In this paper, we develop a growth-rotation search model for characterizing microtubule search for kinetochores, based on a nonlocal generalized polymerization/depolymerization

model combined with a normal rotational diffusion process. Using the established model, we derive the macroscopic equation governing the position distribution of the microtubule tip. Furthermore, by incorporating the 3-dimensional normal diffusion process of kinetochores and imposing absorbing boundary conditions according to the capture condition, we obtain the macroscopic equation for microtubule-kinetochore capture. To investigate additional dynamic properties of the microtubule's tip during the growth-rotation search process, we derive the Feynman-Kac equations satisfied by the probability density of the tip's position functional. Finally, we demonstrate several applications of the derived equations, including the probability density of the rotation-growth model, microtubule-kinetochore capture, the occupation time of the microtubule tip in the interest region, and the joint distribution of position and integral functional. For these applications, the results obtained by directly solving the equations via deep learning method show good match with the approximate probability densities obtained by the particle trajectory simulations using the Monte Carlo method. Thus, the correctness of the derived equations is verified. We provide a more real/practical model for the microscale dynamics of microtubule-kinetochore capture, offering a novel approach to investigate the mechanisms of mitosis. Owing to the high flexibility of this model, it is feasible to integrate deep learning techniques with experimental observation data sets to obtain parameters that better reflect real-world scenarios, thereby simulating mitotic processes with greater realism. This will be considered in our future work.

DATA AVAILABILITY STATEMENT

The data that support the findings of this study are available on request from the corresponding author.

Appendix A: Spherical harmonics

Define the inner product on the unit sphere $\mathbb{S}^2$ as

$$\langle u,v\rangle_{L^2(\mathbb{S}^2)}=\int_0^{2\pi}\int_0^{\pi}\overline{u(\theta,\phi)}v(\theta,\phi)\sin\theta d\theta d\phi,$$

which induces the L^2 norm $\|u\|_{L^2(\mathbb{S}^2)}=\sqrt{\langle u,u\rangle}$. We introduce the spherical harmonics[43], defined as

$$Y_{lm}(\theta,\phi)=\sqrt{\frac{(2l+1)(l-m)!}{4\pi(l+m)!}}P_{lm}(\cos\theta)e^{im\phi},$$

where $P_{lm}(z)$ are the associated Legendre functions, and $m\in\mathbb{Z}$ and $l\in\mathbb{N}$ are two parameters of the polynomial. A function $u(\theta,\phi)\in L^2(\mathbb{S}^2)$ can be represented by spherical harmonics as[43]

$$u(\theta,\phi)=\sum_{l=0}^{\infty}\sum_{m=-l}^{l}\tilde{u}(l,m)Y_{lm}(\theta,\phi),$$

where $\tilde{u}(l,m)$ are the weights. These weights can be calculated by the spherical harmonic transform

$$\tilde{u}(l,m)=\int_0^{2\pi}\int_0^{\pi}u(\theta,\phi)Y_{lm}^*(\theta,\phi)\sin\theta d\theta d\phi,$$

where $Y_{lm}^*(\theta,\phi)=(-1)^mY_{l\{-m\}}(\theta,\phi)$ is the complex conjugate of $Y_{lm}(\theta,\phi)$.

Appendix B: Derivation of (21)

By using Taylor's expansion, we have

$$\begin{aligned}
&\tilde{u}(l,m,s+ds)-\tilde{u}(l,m,s)\\
=&\mathbb{E}\left[Y_{lm}^*(\theta(s),\phi(s))\cos\theta(s)d\theta(s)\right]-\frac{1}{2}\mathbb{E}\left[Y_{lm}^*(\theta(s),\phi(s))\sin\theta(s)(d\theta(s))^2\right]\\
&+\mathbb{E}\left[\left(\frac{\partial}{\partial\theta}Y_{lm}^*(\theta(s),\phi(s))d\theta(s)+\frac{\partial}{\partial\phi}Y_{lm}^*(\theta(s),\phi(s))d\phi(s)\right)\sin\theta(s)\right]\\
&+\mathbb{E}\left[\left(\frac{\partial}{\partial\theta}Y_{lm}^*(\theta(s),\phi(s))d\theta(s)+\frac{\partial}{\partial\phi}Y_{lm}^*(\theta(s),\phi(s))d\phi(s)\right)\cos\theta(s)d\theta(s)\right]\\
&+\frac{1}{2}\mathbb{E}\left[[d\theta(s),d\phi(s)]\,\mathrm{Hess}_{\theta,\phi}(Y_{lm}^*(\theta(s),\phi(s)))\,[d\theta(s),d\phi(s)]^T\sin\theta(s)\right]\\
=&\mathrm{I}+\mathrm{II}+\mathrm{III}+\mathrm{IV}+\mathrm{V}.
\end{aligned}\tag{B1}$$

Then, using the definition (19) and the properties of Brownian motion in (5), one can calculate the five terms on the right-hand side of (B1) as

$$\mathrm{I}=\frac{1}{2}\mathbb{E}\left[\frac{\cos^2\theta}{\sin^2\theta}Y_{lm}^*(\theta(s),\phi(s))\sin\theta(s)ds\right]=\frac{1}{2}\mathscr{F}_{l,m}\left\{\frac{\cos^2\theta}{\sin^2\theta}u(\theta,\phi,s)\right\}ds,$$

$$\mathrm{II} = -\frac{1}{2}\mathbb{E}[Y^*_{lm}(\theta(s),\phi(s))\sin\theta(s)ds] = -\frac{1}{2}\mathscr{F}_{l,m}\{u(\theta,\phi,s)\}ds,$$

$$\begin{aligned}
\mathrm{III} =& \mathbb{E}\left[\frac{\partial}{\partial\theta}Y^*_{lm}(\theta(s),\phi(s))\sin\theta(s)d\theta(s)\right] + \mathbb{E}\left[\frac{\partial}{\partial\phi}Y^*_{lm}(\theta(s),\phi(s))\sin\theta(s)d\phi(s)\right]\\
=& \frac{1}{2}\mathbb{E}\left[\frac{\partial}{\partial\theta}Y^*_{lm}(\theta(s),\phi(s))\sin\theta(s)\frac{\cos\theta(s)}{\sin\theta(s)}ds\right]\\
=& \frac{1}{2}\int_0^{2\pi}\int_0^{\pi}\frac{\partial}{\partial\theta}Y^*_{lm}(\theta,\phi)\cos\theta u(\theta,\phi,s)d\theta d\phi ds\\
=& -\frac{1}{2}\int_0^{2\pi}\int_0^{\pi}Y^*_{lm}(\theta,\phi)\frac{\partial}{\partial\theta}(\cos\theta u(\theta,\phi,s))d\theta d\phi ds\\
=& \frac{1}{2}\int_0^{2\pi}\int_0^{\pi}Y^*_{lm}(\theta,\phi)\sin\theta u(\theta,\phi,s)d\theta d\phi ds - \frac{1}{2}\int_0^{2\pi}\int_0^{\pi}Y^*_{lm}(\theta,\phi)\cos\theta\frac{\partial}{\partial\theta}u(\theta,\phi,s)d\theta d\phi ds\\
=& \frac{1}{2}\mathscr{F}_{l,m}\{u(\theta,\phi,s)\}ds - \frac{1}{2}\mathscr{F}_{l,m}\left\{\frac{\cos\theta}{\sin\theta}\frac{\partial}{\partial\theta}u(\theta,\phi,s)\right\}ds,
\end{aligned}$$

$$\begin{aligned}
\mathrm{IV} =& \mathbb{E}\left[\frac{\partial}{\partial\theta}Y^*_{lm}(\theta(s),\phi(s))\cos\theta(s)(d\theta(s))^2\right]\\
=& \mathbb{E}\left[\frac{\partial}{\partial\theta}Y^*_{lm}(\theta(s),\phi(s))\cos\theta(s)\right]ds\\
=& \mathscr{F}_{l,m}\{u(\theta,\phi,s)\}ds - \mathscr{F}_{l,m}\left\{\frac{\cos\theta}{\sin\theta}\frac{\partial}{\partial\theta}u(\theta,\phi,s)\right\}ds,
\end{aligned}$$

and

$$\begin{aligned}
\mathrm{V} =& \frac{1}{2}\mathbb{E}\left[\frac{\partial^2}{\partial\theta^2}Y^*_{lm}(\theta(s),\phi(s))(d\theta(s))^2\sin\theta(s)\right] + \mathbb{E}\left[\frac{\partial^2}{\partial\theta\partial\phi}Y^*_{lm}(\theta(s),\phi(s))d\theta(s)d\phi(s)\sin\theta(s)\right]\\
&+\frac{1}{2}\mathbb{E}\left[\frac{\partial^2}{\partial\phi^2}Y^*_{lm}(\theta(s),\phi(s))(d\phi(s))^2\sin\theta(s)\right]\\
=& \frac{1}{2}\int_0^{2\pi}\int_0^{\pi}\frac{\partial^2}{\partial\theta^2}Y^*_{lm}(\theta,\phi)\sin\theta u(\theta,\phi,s)d\theta d\phi ds + \frac{1}{2}\int_0^{2\pi}\int_0^{\pi}\frac{\partial^2}{\partial\phi^2}Y^*_{lm}(\theta,\phi)\frac{1}{\sin\theta}u(\theta,\phi,s)d\theta d\phi ds\\
=& -\frac{1}{2}\int_0^{2\pi}\int_0^{\pi}\frac{\partial}{\partial\theta}Y^*_{lm}(\theta,\phi)\frac{\partial}{\partial\theta}(\sin\theta u(\theta,\phi,s))d\theta d\phi ds - \frac{1}{2}\int_0^{2\pi}\int_0^{\pi}\frac{\partial}{\partial\phi}Y^*_{lm}(\theta,\phi)\frac{1}{\sin\theta}\frac{\partial}{\partial\phi}u(\theta,\phi,s)d\theta d\phi ds\\
=& -\frac{1}{2}\int_0^{2\pi}\int_0^{\pi}\frac{\partial}{\partial\theta}Y^*_{lm}(\theta,\phi)\cos\theta u(\theta,\phi,s)d\theta d\phi ds - \frac{1}{2}\int_0^{2\pi}\int_0^{\pi}\frac{\partial}{\partial\theta}Y^*_{lm}(\theta,\phi)\sin\theta\frac{\partial}{\partial\theta}u(\theta,\phi,s)d\theta d\phi ds\\
&+\frac{1}{2}\int_0^{2\pi}\int_0^{\pi}Y^*_{lm}(\theta,\phi)\frac{1}{\sin\theta}\frac{\partial^2}{\partial\phi^2}u(\theta,\phi,s)d\theta d\phi ds\\
=& \frac{1}{2}\int_0^{2\pi}\int_0^{\pi}Y^*_{lm}(\theta,\phi)\frac{\partial}{\partial\theta}(\cos\theta u(\theta,\phi,s))d\theta d\phi ds + \frac{1}{2}\int_0^{2\pi}\int_0^{\pi}Y^*_{lm}(\theta,\phi)\frac{\partial}{\partial\theta}(\sin\theta\frac{\partial}{\partial\theta}u(\theta,\phi,s))d\theta d\phi ds\\
&+\frac{1}{2}\mathscr{F}_{l,m}\left\{\frac{1}{\sin^2\theta}\frac{\partial^2}{\partial\phi^2}u(\theta,\phi,s)\right\}ds\\
=& -\frac{1}{2}\int_0^{2\pi}\int_0^{\pi}Y^*_{lm}(\theta,\phi)\sin\theta u(\theta,\phi,s)d\theta d\phi\cdot ds + \int_0^{2\pi}\int_0^{\pi}Y^*_{lm}(\theta,\phi)\cos\theta\frac{\partial}{\partial\theta}u(\theta,\phi,s)d\theta d\phi ds\\
&+\frac{1}{2}\int_0^{2\pi}\int_0^{\pi}Y^*_{lm}(\theta,\phi)\sin\theta\frac{\partial^2}{\partial\theta^2}u(\theta,\phi,s)d\theta d\phi ds + \frac{1}{2}\mathscr{F}_{l,m}\left\{\frac{1}{\sin^2\theta}\frac{\partial^2}{\partial\phi^2}u(\theta,\phi,s)\right\}ds\\
=& -\frac{1}{2}\mathscr{F}_{l,m}\{u(\theta,\phi,s)\}ds + \mathscr{F}_{l,m}\left\{\frac{\cos\theta}{\sin\phi}\frac{\partial}{\partial\theta}u(\theta,\phi,s)\right\}ds + \frac{1}{2}\mathscr{F}_{l,m}\left\{\frac{\partial^2}{\partial\theta^2}u(\theta,\phi,s)\right\}ds\\
&+\frac{1}{2}\mathscr{F}_{l,m}\left\{\frac{1}{\sin^2\theta}\frac{\partial^2}{\partial\phi^2}u(\theta,\phi,s)\right\}ds.
\end{aligned}$$

Adding the above five parts together yields

$$\tilde{u}(l,m,s+ds)-\tilde{u}(l,m,s)=\frac{1}{2}\mathscr{F}_{l,m}\left\{\frac{1}{\sin^2\theta}u(\theta,\phi,s)-\frac{\cos\theta}{\sin\theta}\frac{\partial}{\partial\theta}u(\theta,\phi,s)+\frac{\partial}{\partial\theta^2}u(\theta,\phi,s)+\frac{1}{\sin^2\theta}\frac{\partial}{\partial\phi^2}u(\theta,\phi,s)\right\}ds.$$

Appendix C: Derivation of (39)

Using the double expectation formula, we have

$$\begin{aligned}
&\tilde{u}(r,l,m,p,t+dt)\\
=&\mathbb{E}\left[\mathbb{I}_{\{r(t+dt)\}}Y^*_{lm}(\theta(t+dt),\phi(t+dt))\sin\theta(t+dt)e^{-ipA(t+dt)}\right]\\
=&\mathbb{E}\left[\mathbb{I}_{\{r(t+dt)\}}\mathbb{E}\left[Y^*_{lm}(\theta(t+dt),\phi(t+dt))\sin\theta(t+dt)e^{-ipA(t+dt)};r(t+dt)\right]\right]\\
=&\mathbb{E}\left[\mathbb{I}_{\{r(t+dt)\}}\mathbb{E}\left[Y^*_{lm}(\theta(t+dt),\phi(t+dt))\sin\theta(t+dt)e^{-ipA(t+dt)};r(t)\right]\right].
\end{aligned}$$

By using the definition (8), the properties of Brownian motion in (5), Taylor's expansion, and following the derivation analogous to that of (B1), we have

$$\begin{aligned}
&F(r(t))\\
:=&\mathbb{E}\left[Y^*_{lm}(\theta(t+dt),\phi(t+dt))\sin\theta(t+dt)e^{-ipA(t+dt)};r(t)\right]\\
=&\mathbb{E}\left[Y^*_{lm}(\theta(t),\phi(t))\sin\theta(t)e^{-ipA(t)};r(t)\right]+\mathbb{E}\left[Y^*_{lm}(\theta(t),\phi(t))\cos\theta(t)d\theta(t);r(t)\right]\\
&-\frac{1}{2}\mathbb{E}\left[Y^*_{lm}(\theta(t),\phi(t))\sin\theta(t)e^{-ipA(t)}(d\theta(t))^2;r(t)\right]+\mathbb{E}\left[\frac{\partial}{\partial\theta}Y^*_{lm}(\theta(t),\phi(t))\sin\theta(t)e^{-ipA(t)}d\theta(t);r(t)\right]\\
&+\mathbb{E}\left[\frac{\partial}{\partial\phi}Y^*_{lm}(\theta(t),\phi(t))\sin\theta(t)e^{-ipA(t)}d\phi(t);r(t)\right]+\mathbb{E}\left[\frac{\partial}{\partial\theta}Y^*_{lm}(\theta(t),\phi(t))\cos\theta(t)e^{-ipA(t)}(d\theta(t))^2;r(t)\right]\\
&+\mathbb{E}\left[\frac{\partial}{\partial\phi}Y^*_{lm}(\theta(t),\phi(t))\cos\theta(t)e^{-ipA(t)}d\phi(t)d\theta(t);r(t)\right]+\frac{1}{2}\mathbb{E}\left[\frac{\partial^2}{\partial\theta^2}Y^*_{lm}(\theta(t),\phi(t))\sin\theta(t)e^{-ipA(t)}(d\theta(t))^2;r(t)\right]\\
&+\mathbb{E}\left[\frac{\partial^2}{\partial\phi\partial\theta}Y^*_{lm}(\theta(t),\phi(t))\sin\theta(t)e^{-ipA(t)}d\phi(t)d\theta(t);r(t)\right]+\frac{1}{2}\mathbb{E}\left[\frac{\partial^2}{\partial\phi^2}Y^*_{lm}(\theta(t),\phi(t))\sin\theta(t)e^{-ipA(t)}(d\phi(t))^2;r(t)\right]\\
&-ip\mathbb{E}\left[U(r(t)x(\theta(t),\phi(t)))Y^*_{lm}(\theta(t),\phi(t))\sin\theta(t)e^{-ipA(t)};r(t)\right]\\
=&\mathscr{F}_{l,m}\left\{\tilde{u}(\theta,\phi,p,t;r(t))+\frac{D_x}{r(t)^2}\tilde{\Delta}_S\tilde{u}(\theta,\phi,p,t;r(t))dt-ipU(r(t)x(\theta,\phi))\tilde{u}(\theta,\phi,p,t;r(t))dt\right\}.
\end{aligned}$$

Based on the transition probability of $r(t)$ defined in (3), one can obtain

$$
\begin{aligned}
&\tilde{u}(r,l,m,p,t+dt)\\
=&\mathbb{E}\left[\mathbb{I}_{\{r(t+dt)\}}F(r(t))\right]\\
=&\mathbb{E}\left[\sum_{k=1}^{r(t)-r_{\min}}\mu_k(r(t))\mathbb{I}_{\{r(t)-k=r\}}F(r(t))dt+\sum_{k=1}^{r_{\max}-r(t)}\lambda_k(r(t))\mathbb{I}_{\{r(t)+k=r\}}F(r(t))dt\right.\\
&\left.+\left(1-\sum_{k=1}^{r(t)-r_{\min}}\mu_k(r(t))dt-\sum_{k=1}^{r_{\max}-r(t)}\lambda_k(r(t))dt\right)\mathbb{I}_{\{r(t)=r\}}F(r(t))\right]\\
=&\sum_{i=r_{\min}}^{r_{\max}}\left(\sum_{k=1}^{i-r_{\min}}\mu_k(i)\mathbb{I}_{\{i-k=r\}}F(i)dt+\sum_{k=1}^{r_{\max}-i}\lambda_k(i)\mathbb{I}_{\{i+k=r\}}F(i)dt+\left(1-\sum_{k=1}^{i-r_{\min}}\mu_k(i)dt-\sum_{k=1}^{r_{\max}-i}\lambda_k(i)dt\right)\mathbb{I}_{\{i=r\}}F(i)\right)u(i,t)\\
=&\sum_{k=r+1}^{r_{\max}}\mu_{k-r}(k)F(k)u(k,t)dt+\sum_{k=r_{\min}}^{r-1}\lambda_{r-k}(k)F(k)u(k,t)dt-\left(\sum_{k=1}^{r-r_{\min}}\mu_k(r)+\sum_{k=1}^{r_{\max}-r}\lambda_k(r)\right)F(r)u(r,t)dt+F(r)u(r,t)\\
=&\sum_{k=1}^{r_{\max}-r}\mu_k(r+k)F(r+k)u(r+k,t)dt+\sum_{k=1}^{r-r_{\min}}\lambda_k(r-k)F(r-k)u(r-k,t)dt\\
&-\left(\sum_{k=1}^{r-r_{\min}}\mu_k(r)+\sum_{k=1}^{r_{\max}-r}\lambda_k(r)\right)F(r)u(r,t)dt+F(r)u(r,t)\\
=&\tilde{u}(r,l,m,p,t)+L_r\tilde{u}(r,l,m,p,t)dt+\mathscr{F}_{l,m}\left\{\frac{D_x}{r^2}\tilde{\Delta}_S\tilde{u}(r,\theta,\phi,p,t)-ipU(rx(\theta,\phi))\tilde{u}(r,\theta,\phi,p,t)\right\}dt.
\end{aligned}
$$

Appendix D: Derivation of (44)

Using the double expectation formula, the transition probability (3), Taylor's expansion, and the properties of the Brownian motion in (5), we have

$$
\begin{aligned}
&\mathbb{E}\left[\tilde{u}_{r|_{r_0(dt)},\theta|_{\theta_0(dt)},\phi|_{\phi_0(dt)}}(p,t)\right]\\
=&\tilde{u}_{r_0,\theta_0,\phi_0}(p,t)+\sum_{k=1}^{r_0-r_{\min}}\mu_k(r_0)\tilde{u}_{r_0-k,\theta_0,\phi_0}(p,t)dt+\sum_{k=1}^{r_{\max}-r_0}\lambda_k(r_0)\tilde{u}_{r_0+k,\theta_0,\phi_0}(p,t)dt\\
&-\left(\sum_{k=1}^{r_0-r_{\min}}\mu_k(r_0)+\sum_{k=1}^{r_{\max}-r_0}\lambda_k(r_0)\right)\tilde{u}_{r_0,\theta_0,\phi_0}(p,t)dt+\frac{D_x}{r_0^2}\left(\frac{\cos\theta_0}{\sin\theta_0}\frac{\partial}{\partial\theta_0}\tilde{u}_{r_0,\theta_0,\phi_0}(p,t)+\frac{\partial^2}{\partial\theta_0^2}\tilde{u}_{r_0,\theta_0,\phi_0}(p,t)\right.\\
&\left.+\frac{1}{\sin^2\theta_0}\frac{\partial^2}{\partial\phi_0^2}\tilde{u}_{r_0,\theta_0,\phi_0}(p,t)\right)dt\\
=&\tilde{u}_{r_0,\theta_0,\phi_0}(p,t)+F_{r_0}\tilde{u}_{r_0,\theta_0,\phi_0}(p,t)dt+\frac{D_x}{r_0^2}\Delta_S\tilde{u}_{r_0,\theta_0,\phi_0}(p,t)dt.
\end{aligned}
$$

ACKNOWLEDGMENTS

This work was supported by the National Natural Science Foundation of China under Grant No. 12225107, the Major Science and Technology Projects in Gansu Province-Leading Talents in Science and Technology under Grant No. 23ZDKA0005, the Gansu Province Postgraduate Innovation Star Program No. 2025CXZX-151, the Joint Scientific Research Fund of Gansu Provincial Science and Technology Plan Nos. 25JRRA1254 and 25JRRA1255, and Lanzhou Talent Work Special Fund.

REFERENCES

[1] T. Mitchison and M. Kirschner, Nature **312**, 237 (1984).
[2] T. E. Holy and S. Leibler, Proc. Natl. Acad. Sci. USA **91**, 5682 (1994).
[3] R. Wollman, E. N. Cytrynbaum, J. T. Jones, T. Meyer, J. M. Scholey, and A. Mogilner, Curr. Biol. **15**, 828 (2005).
[4] R. Paul, R. Wollman, W. T. Silkworth, I. K. Nardi, D. Cimini, and A. Mogilner, Proc. Natl. Acad. Sci. USA **106**, 15708 (2009).
[5] I. Kalinina, A. Nandi, P. Delivani, M. R. Chacón, A. H. Klemm, D. Ramunno-Johnson, A. Krull, B. Lindner, N. Pavin, and I. M. Tolić-Nørrelykke, Nat. Cell Biol. **15**, 82 (2013).

[6]R. Blackwell, O. Sweezy-Schindler, C. Edelmaier, Z. R. Gergely, P. J. Flynn, S. Montes, A. Crapo, A. Doostan, J. R. McIntosh, M. A. Glaser, et al., Biophys. J. **112**, 552 (2017).
[7]I. Nayak, D. Das, and A. Nandi, Phys. Rev. Res. **2**, 013114 (2020).
[8]G. G. and S. J. M., Annu. Rev. Cell Dev. Biol. **26** (2010).
[9]F. J. McNally and R. D. Vale, Cell **75**, 419 (1993).
[10]A. Khodjakov, L. Copenagle, M. B. Gordon, D. A. Compton, and T. M. Kapoor, J. Cell Biol. **160**, 671 (2003).
[11]T. Zhou, H. Wang, and W. H. Deng, J. Phys. A: Math. Theor. **57**, 285001 (2024).
[12]X. Zhang, H. Wang, and W. H. Deng, Chaos **34**, 123144 (2024), ISSN 1054-1500.
[13]X. Y. Wu, D. X. Nie, and W. H. Deng, Chaos **35**, 033117 (2025), ISSN 1054-1500.
[14]H. Wang and W. H. Deng, J. Mach. Learn. **3**, 215 (2024), ISSN 2790-2048.
[15]K. Arif, G. J. Xi, H. Wang, and W. H. Deng, J. Comput. Phys. p. 114327 (2025), ISSN 0021-9991.
[16]M. Raissi, P. Perdikaris, and G. E. Karniadakis, J. Comput. Phys. **378**, 686 (2019), ISSN 0021-9991.
[17]W. E and B. Yu, Commun. Math. Stat. **6** (2018).
[18]Y. Zang, G. Bao, X. Ye, and H. Zhou, J. Comput. Phys. **411**, 109409 (2020), ISSN 0021-9991.
[19]J. Han, A. Jentzen, and W. E, Proc. Natl. Acad. Sci. USA **115**, 8505 (2018).
[20]L. T. Ferreira and H. Maiato, Semin. Cell Dev. Biol. **117**, 52 (2021), ISSN 1084-9521.
[21]J. Gautier, C. Norbury, M. Lohka, P. Nurse, and J. Maller, Cell **54** (1988).
[22]M. J. Lohka, M. K. Hayes, and J. L. Maller, Proc. Natl. Acad. Sci. USA **85**, 3009 (1988).
[23]S. Moutinho-Pereira, N. Stuurman, O. Afonso, M. Hornsveld, P. Aguiar, G. Goshima, R. D. Vale, and H. Maiato, Proc. Natl. Acad. Sci. USA **110** (2013).
[24]H. Maiato, A. M. Gomes, F. Sousa, and M. Barisic, Biology **6** (2017), ISSN 2079-7737.
[25]D. Cimini, L. A. Cameron, and E. D. Salmon, Curr. Biol. **14**, 2149 (2004).
[26]D. J. Tomkins and J. E. Sisken, Am. J. Hum. Genet. **36**, 1332 (1984).
[27]C. Y. Hung, B. Volkmar, J. D. Baker, J. W. Bauer, E. Gussoni, S. Hainzl, A. Klausegger, J. Lorenzo, I. Mihalek, O. Rittinger, et al., PLOS ONE **12**, 1 (2017).
[28]D. Hanahan and R. A. Weinberg, Cell **144**, 646 (2011).
[29]J. C. Macedo, S. Vaz, B. Bakker, R. Ribeiro, P. L. Bakker, J. M. Escandell, M. G. Ferreira, R. Medema, F. Foijer, and E. Logarinho, Nat. Commun. **9**, 2834 (2018).
[30]R. A. Walker, E. T. O'Brien, N. K. Pryer, M. F. Soboeiro, W. A. Voter, H. P. Erickson, and E. D. Salmon, J. Cell Biol. **107**, 1437 (1988).
[31]I. Kalinina, A. Nandi, P. Delivani, et al., Nat. Cell Biol. **15**, 82 (2013).
[32]H. Wang, X. H. Li, L. J. Zhao, and W. H. Deng, Fundam. Res. (2025), ISSN 2667-3258.
[33]A. V. Chechkin, F. Seno, R. Metzler, and I. M. Sokolov, Phys. Rev. X **7**, 021002 (2017).
[34]B. Wang, S. M. Anthony, S. C. Bae, and S. Granick, Proc. Natl. Acad. Sci. USA **106**, 15160 (2009).
[35]F. Baldovin, E. Orlandini, and F. Seno, Front. Phys. **7** (2019), ISSN 2296-424X.
[36]S. Nampoothiri, E. Orlandini, F. Seno, and F. Baldovin, New J. Phys. **24**, 023003 (2022).
[37]H. Risken, *The Fokker-Planck Equation*, Springer Series in Synergetics (Springer Berlin, Heidelberg, 1996).
[38]E. Barkai and R. J. Silbey, The Journal of Physical Chemistry B **104**, 3866 (2000).
[39]L. Turgeman, S. Carmi, and E. Barkai, Phys. Rev. Lett. **103**, 190201 (2009).
[40]A. Cairoli and A. Baule, Phys. Rev. Lett. **115**, 110601 (2015).
[41]A. Cairoli and A. Baule, J. Phys. A: Math. Theor. **50**, 164002 (2017).
[42]H. Wang and W. H. Deng, *Deep learning for high-dimensional PDEs on manifold with Neumann and Dirichlet boundary conditions* (2025), in press.
[43]B. Rafaely, *Fundamentals of Spherical Array Processing*, no. 2 in Springer Topics in Signal Processing (Springer Cham, 2019), ISBN 978-3-319-99560-1, 978-3-030-07611-5, 978-3-319-99561-8.
[44]W. H. Deng, X. C. Wu, and W. L. Wang, Europhys. Lett. **117**, 10009 (2017).
[45]X. D. Wang, Y. Chen, and W. H. Deng, Phys. Rev. E **98**, 052114 (2018).
[46]G. Foltin, K. Oerding, Z. Rácz, R. L. Workman, and R. K. P. Zia, Phys. Rev. E **50**, R639 (1994).
[47]G. Hummer and A. Szabo, Proc. Natl. Acad. Sci. USA **98**, 3658 (2001).
[48]A. Comtet, J. Desbois, and C. Texier, J. Phys. A **38**, R341 (2005).
[49]A. Baule and R. Friedrich, Phys. Lett. A **350**, 167 (2006), ISSN 0375-9601.
[50]S. N. Majumdar and A. J. Bray, Phys. Rev. E **65**, 051112 (2002).
[51]A. Comtet, C. Monthus, and M. Yor, J. Appl. Probab. **35**, 255 (1998).